inorganics

MDPI

Article

Matrix Effect on Singlet Oxygen Generation Using Methylene Blue as Photosensitizer

Jianan Xu [1], Laurent Bonneviot [1], Yannick Guari [2], Cyrille Monnereau [1], Kun Zhang [3], Albert Poater [4], Montserrat Rodríguez-Pizarro [4,*] and Belén Albela [1,*]

1 Laboratoire de Chimie, Ecole Normale Supérieure de Lyon—CNRS UMR51, 69364 Lyon, France; jianan.xu@ens-lyon.fr (J.X.); laurent.bonneviot@ens-lyon.fr (L.B.); cyrille.monnereau@ens-lyon.fr (C.M.)
2 Institut Charles Gerhardt Montpellier, University Montpellier, CNRS, Ecole Nationale Supérieure de Chimie de Montpellier, 34293 Montpellier, France; yannick.guari@umontpellier.fr
3 Shanghai Key Laboratory of Green Chemistry and Chemical Processes, East China Normal University, Shanghai 200062, China; kzhang@chem.ecnu.edu.cn
4 Departament de Química and Institut de Química Computacional i Catàlisi, Facultat de Ciències, Universitat de Girona, 17003 Girona, Spain; albert.poater@udg.edu
* Correspondence: montse.rodriguez@udg.edu (M.R.-P.); belen.albela@ens-lyon.fr (B.A.)

Abstract: Methylene blue (MB) is a well-established and extensively studied photosensitizer for photodynamic therapy (PDT), since it can generate singlet oxygen with a high quantum yield upon irradiation within the phototherapeutic (600–950 nm) window. However, its activity can decrease due to the formation of dimers or higher aggregates, which can take place in an aqueous solution at relatively high concentrations. The incorporation of this molecule into a matrix can avoid this aggregation and increase its activity relative to PDT. Silica porous nanoparticles are chosen here as a matrix to host MB. The size and pore geometry are tuned in order to decrease MB leaching while maintaining good singlet oxygen generation and colloidal stability for further applications in nanomedicine. In addition, phenyl functions are grafted on the pores of the silica matrix in order to avoid MB aggregation, thereby increasing the activity of the photosensitizer in the singlet oxygen generation. DFT calculations give insight in the structure of the aggregation of the MB units, and the roles of water and organic environments are investigated through time-dependent calculations on UV-vis spectra.

Keywords: silica nanoparticles; methylene blue; singlet oxygen generation; photodynamic therapy

check for updates

Citation: Xu, J.; Bonneviot, L.; Guari, Y.; Monnereau, C.; Zhang, K.; Poater, A.; Rodríguez-Pizarro, M.; Albela, B. Matrix Effect on Singlet Oxygen Generation Using Methylene Blue as Photosensitizer. *Inorganics* **2024**, *12*, 155. https://doi.org/10.3390/inorganics12060155

Academic Editor: Bernhard Spingler

Received: 24 April 2024
Revised: 28 May 2024
Accepted: 28 May 2024
Published: 31 May 2024

Copyright: © 2024 by the authors. Licensee MDPI, Basel, Switzerland. This article is an open access article distributed under the terms and conditions of the Creative Commons Attribution (CC BY) license (https://creativecommons.org/licenses/by/4.0/).

1. Introduction

Cancer has become one of the leading reasons of mortality throughout the world, causing millions of deaths annually [1,2]. Nowadays, traditional therapies such as chemotherapy and radiotherapy mainly are still applied for the clinical treatment of cancer. However, the disadvantages of traditional therapies, i.e., poor selectivity, low curative effect, strong toxic side effects, and painful procedures, hinder their extensive clinical application. Compared with these conventional therapies, photodynamic therapy (PDT) is an alternative approach for cancer treatment which displays desirable properties such as low systemic toxicity and minimal invasiveness [3].

PDT involves three key components, namely, a photosensitizer (PS), a specific wavelength of light, and oxygen (O_2), the ground state of it being triplet oxygen ($^3O_2$). PDT can be divided into two types (Type I and Type II) [4,5]. Under light irradiation, the PSs at ground singlet state can be first promoted to an excited singlet state and then go through intersystem crossing (ISC) to reach a triplet state. For Type-I PDT, triplet PSs can generate free radicals via hydrogen abstraction or electron transfer with surrounding substrates [6], while for Type-II PDT, triplet state PS transfers energy to molecular oxygen directly to form cytotoxic singlet oxygen ($^1O_2$) [7,8]. Indeed, in Type I, generated cytotoxic reactive oxygen

species (ROS), including H_2O_2, $^{\bullet}OH$, and $O_2^{\bullet-}$, can stimulate cell apoptosis or necrosis, vascular damage, and immune activation [3,7]. As it happens, Type I is not considered to be the main mechanism for most applications of PDT. Therefore, our research focuses mainly on PSs that allow for the Type II mechanism.

Methylene blue (MB) is a convenient PS due to its solubility in water. It is able to generate singlet oxygen with relatively high quantum yield (Φ_{Δ}~0.5) and demonstrates strong electrophilic activation of oxidizing electron-rich double bonds in biological molecules and macromolecules [9]. Recent studies have suggested that MB has beneficial effects on memory improvement and Alzheimer's disease [10]. Currently, it is used clinically in a wide range of medications that treat conditions such as methemoglobinemia, urinary tract infections, plaque psoriasis, thyroid surgery, cancer chemotherapy, and ifosfamide-induced encephalopathy [10].

MB undergoes a well-known dimerization process in solution [11], which reaches a significant extent in polar environments, and above concentrations of ca. 10^{-5} M. This represents a drawback for the generation of singlet oxygen (Type II mechanism), as dimers follow in most cases an electron-transfer (Type I) pathway for deactivation, with almost complete abolition of singlet oxygen generation, except for a few systems under very specific conditions [12]. Thus, the design of systems that allow the occurrence of the MB monomeric form is preferred. The high quantum yield of $^1O_2$ generation, coupled with a relatively low dark toxicity [13], makes methylene blue an attractive candidate for PDT. However, clinical use of methylene blue for PDT has been limited, because systemic administration fails to provide significant therapeutic efficacy. MB accumulates extensively in erythrocytes [14] and endothelial cells [15,16], where it is reduced to leucomethylene blue, resulting in the loss of photodynamic activity [17].

Incorporation of MB in a matrix, such as inorganic nanoparticles, is an efficient approach for reducing its degradation in the biological environment and enables greater availability at the tumor tissue [18]. Mesoporous silica nanoparticles (MSNs) are regarded as promising vectors for drug delivery systems due to their large specific surface area, controllable pore size, various morphologies, and satisfaction of biocompatibility and biodegradability requirements [19]. Various photosensitizer–MSNs combinations have already been tested in vivo [20], though a greater control of MSNs' physicochemical characteristics, such as morphology, shape, and particle and pore size is mandatory prior to both a systematic evaluation of long-term toxicity and to their general use in clinical trials [21].

Regarding the functionalization of MSN, it is easy to add specific functions, thanks to the hydroxyl groups present on the silica's surface [22]. For the incorporation of MB, its positively charged nature allows it to bind to negatively-charged silica nanoparticles via electrostatic interactions. Makhadmeh et al. [23] analyzed the physical effects of MB encapsulated within silica nanoparticles (SiNPs) for photodynamic therapy. The results confirmed the applicability of MB encapsulated in SiNPs to the hemolysis of red blood cells (RBCs), and established a relationship between the concentration of the MB encapsulated within the silica nanoparticles and the time required to break 50% of the RBCs (t_{50}). In brief, the MB encapsulated in SiNPs exhibited higher efficacy compared to that of naked MB.

Sun et al. [24] developed MSN surface-enriched composite membranes with remarkable photodynamic antimicrobial activities via a simple electrospinning method. They used a mixture of zein—a biodegradable protein, and polycaprolactone—a biodegradable polyester, as a matrix where MB-loaded mesoporous silica nanoparticles (MSN) modified with heptadecafluorodecyl groups were deposited, acting as an ROS generator and exerting their antimicrobial performance. Owing to their low surface energy, the fluorinated MSN tended to be enriched on the surface of the nanofiber, hence significantly enhancing ROS generation. Yang et al. [25] developed doxorubicin and MB co-loaded diselenide-bond-bridged MSNs to confer light-responsive chemo-photodynamic-immunotherapy for breast cancer. Under low doses of red-light irradiation, the polyethylene glycol (PEG)-modified, diselenide-bridged MSNs not only achieved MB-mediated PDT to induce tumor cell death, but also triggered matrix degradation and drug release via ROS production, leading to the

synergistic chemo-phototherapy of breast cancer and the boosting of immunogenic cell death effects and systematic anti-tumor immunity responses. Seo et al. [26] synthesized MB-loaded gold nanorod@SiO_2 core–shell nanoparticles for their use in cancer imaging and photothermal/photodynamic dual therapy. Encapsulated MB molecules are present under both monomeric and dimeric forms, and this results in an increase of the photosensitizing effect through the different photochemical pathways. As a consequence of the excellent plasmonic properties of gold nanorods at near-infrared (NIR) light, the embedded MB molecules showed NIR light-induced surface-enhanced Raman scattering (SERS) performance.

So far, neither the stability, nor the retention of the photosensitizer (PS) inside the nanoporous silica matrix, nor their effect on the $^1O_2$ generation have been investigated thoroughly. We propose in this work to tackle this issue by choosing methylene blue (MB) as the PS molecule and varying the particle topology, pore array, and composition for a given size of particle. The capacity of the systems here studied to generate singlet oxygen is tested in order to apply these systems to photodynamic therapy; hence, colloidal stability in water and physiological solutions is key.

2. Results and Discussion

2.1. Synthesis of the Silica Nanoparticles

We chose as a matrix silica mesoporous nanoparticles 80–100 nm in diameter, allowing us to design well-defined pore topologies while keeping good control over size. We used electron microscopy (SEM and TEM) as a monitoring characterization tool. The synthetic protocol was adapted from one of our previous works, aiming to generate different pore topologies [27]. Knowing that the synthesis solution is biphasic, that is, mainly aqueous, with hydrophobic droplets of the organic precursor of silica (TEOS), the particle growth relies on a complex process that combines both mass transfer and kinetics. Therefore, reaction time and stirring rate have to be rigorously controlled. In addition, the proportions of the reactants in the initial mixture can be modified. The ratio between the silica source—tetraethyl orthosilicate, TEOS—and the base—triethanolamine, $TEAH_3$—does indeed act on the pore array (i) kinetically, as $TEAH_3$ is a catalyst for silica condensation, and (ii) thermodynamically, via the electrostatic interaction between the cationic surfactant—cetyltrimethylammonium, CTA^+—and the nascent negatively-charged silica oligomers. This interaction between the silica and the surfactant is particularly sensitive to the pH and the nature of the surfactant counterion, here, tosylate or bromide. As a reminder, tosylate counterions develop stronger competition than bromide against the negatively charged silicate, decreasing its electrostatic affinity to organic micelles and favoring a larger pore wall and size, as more than one micelle can template a single pore [27]. Conversely, increasing the amine concentration increases the pH and the negative charge density on the nascent silica, favoring single micelle templating and fewer open pores compared to those of raspberry. And as we shall see below, certain conditions favor a worm-like internal morphology [27].

We adopt here a nomenclature in direct connection with the sample morphology. This is the Shape–Topology–Pore–Array (SToPA) nomenclature previously reported [28]. While the external shape is basically spherical in the present work, the name of the samples will take into account only the pore array—stellate (ST), raspberry (RB), and radial (r)—and the combination (or not) in the uniform (u), core–shell (cs), or core–shell–corona (csc) morphologies encountered in this study.

We first synthesized silica nanoparticles with uniform stellate and raspberry pore morphologies (u-ST and u-RB) of around 90 nm in diameter, showing quite a good dispersion in size and high yields of silica (around 70%) (Figure 1a,b, Table 1). For the raspberry morphology, leaving the nanoparticle suspensions in aqueous solution for some weeks resulted in a diminution of the average particle size, consistent with a partial dissolution of the nanoparticles (particle diameters around 45 nm, Figures S1 and S2). In addition, these particles tended to fuse to each other, resulting in aggregates of smaller particles. In

comparison, stellate morphology is more resistant to dissolution. In order to take advantage of the RB morphology for confinement and the ST for stability, we synthesized core–shell nanoparticles (Figure 1c,d). We planned to compare two different types of core–shell particles by inverting the RB and ST morphologies as core and shell. A simple protocol was put into place by starting both RB and ST syntheses in parallel, and then adding half of the RB reaction mixture into half of the ST mixture and vice versa (see experimental section). This strategy resulted in two materials: (1) core–shell ST/RB, i.e., ST cores surrounded by an RB shell (Figure 2c); and (2) core–shell RB/r, i.e., nanoparticles that possess an RB-type core surrounded by a thin shell, presenting pores that, surprisingly, turned out to be radial (r) pores instead of the expected ST-type (Figure 2d).

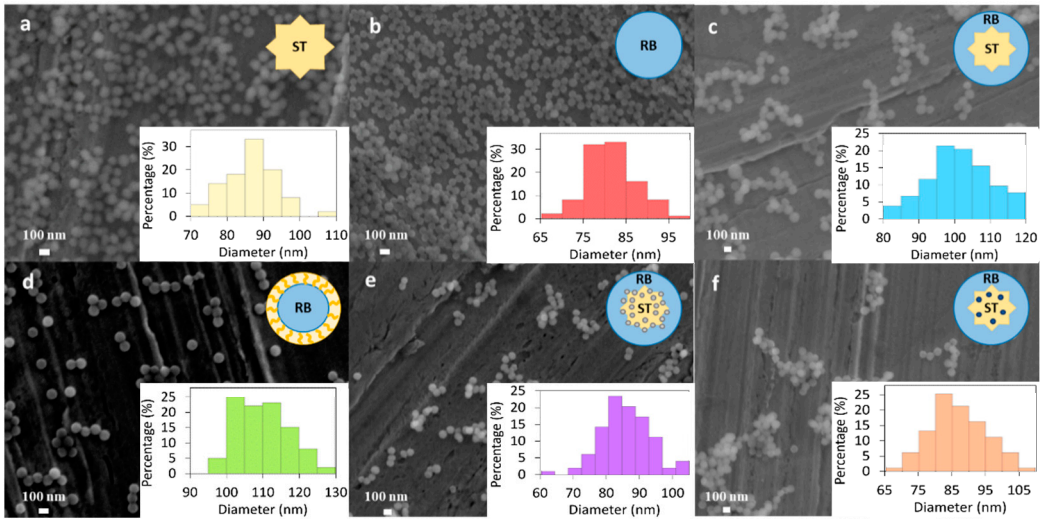

Figure 1. SEM images and particle-size distributions of (**a**,**b**)—uniform ST and RB, (**c**) core–shell ST/RB, (**d**) core–shell RB/r, (**e**) core–shell–corona ST/PhS/RB, and (**f**) RB@(MB@ST) samples. ST = stellate, RB = raspberry, r = radial, PhS = 2-phenylethylsilane.

Finally, phenyl functions were incorporated in RB nanoparticles (Figure 1e) using co-condensation synthesis of TEOS and 2-phenylethyltrimethoxysilane (Ph-silane) [29]. The aims were to both favor the presence of methylene blue monomers and avoid their leaching from the silica matrix by π-π stacking interactions. A molar ratio Ph-silane/TEOS = 0.01 was considered, and the 2-phenylethylsilane precursor was added at the end of the synthesis in order to locate the organic functions preferentially on the external part of the nanoparticle. Our intention was the following: upon delaying the incorporation of the phenyl precursor during the synthesis of the nanoparticles, the phenyl functions should be located close to the exterior. Therefore, the methylene blue molecules should also be located at the particle's periphery. This strategy should optimize the diffusion of the highly reactive singlet oxygen species towards external targets. The synthesis was optimized to obtain a similar particle size, compared to the pure silica nanoparticles. In fact, using the typical conditions to generate u-ST (ø~90 nm) in the presence of 2-phenylethylsilane precursors, we obtained smaller particles with RB morphology (ø~45 nm, Figure S3). In addition, the phenyl groups located on the surface may favor particle aggregation due to π-π stacking. The stirring speed was thus lowered to favor larger particles. TEOS was added again in a final step, in order to minimize the amount of phenyl functions on the surface of the particles and thus avoid particle aggregation in water.

TEM images confirmed the u-ST and u-RB morphologies targeted in the one-step syntheses. As expected, the u-ST morphology shows greater contrast at the core of the particle, where silica density is highest, which is consistent with estuary-like pores that can be schematically represented as cones (Figure 2a). Conversely, u-RB nanoparticles show a uniform silica density corresponding to almost-spherical pores and a narrow pore size distribution of around 3 nm [27,30]. Concerning the core–shell ST/RB sample, ST cores are

indeed covered by a RB shell, giving rise to particles with a more irregular external surface (Figure 2c). On the other hand, core–shell RB/r nanoparticles present a large RB core with a thin radial shell, resulting in spherical, well-defined nanoparticles that are well dispersed, thus demonstrating that a radial thin shell is necessary to increase the colloidal stability of RB nanoparticles and avoid particle merging (Figure 2d).

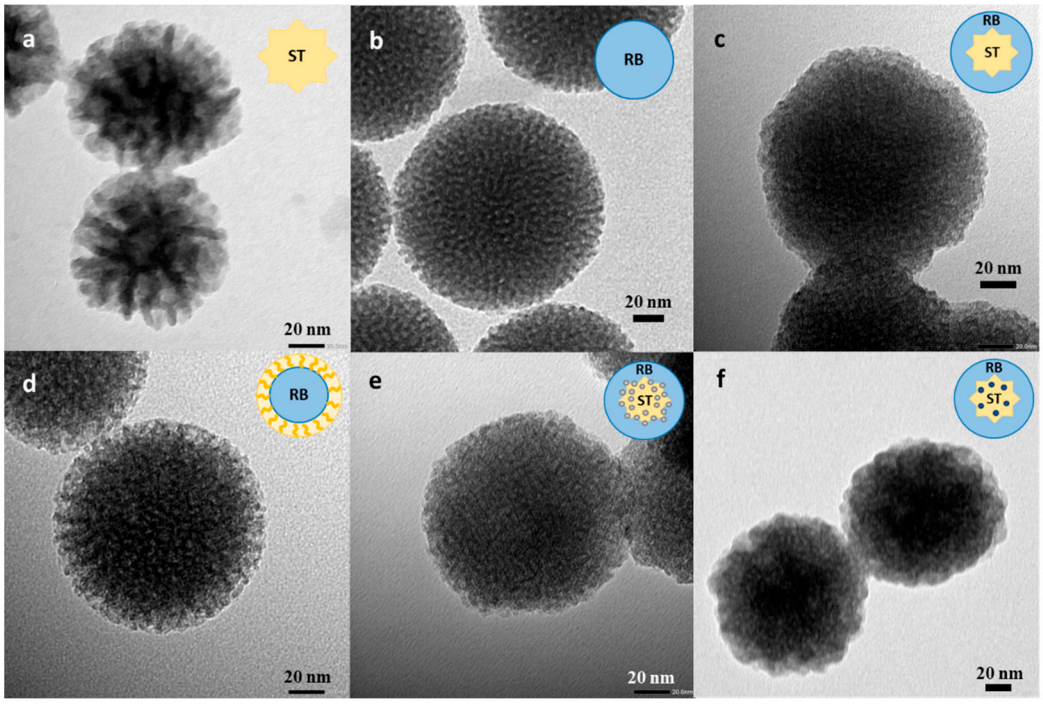

Figure 2. TEM images of (**a**,**b**)—uniform ST and RB, (**c**) core–shell ST/RB, (**d**) core–shell RB/r, (**e**) core–shell–corona ST/PhS/RB, and (**f**) RB@(MB@ST) nanoparticles. ST = stellate, RB = raspberry, r = radial, PhS = 2-phenylethylsilane.

Table 1. Particle-size distribution and methylene blue (MB) retention.

Sample	Size/nm [a]	MB Retention (%) [b]
MB@u-ST	86 ± 7	100
MB@u-RB	81 ± 6	67
MB@cs-RB/r	108 ± 7	81
MB@cs-ST/RB	99 ± 9	100
MB@csc-ST/PhS/RB	91 ± 9	100
RB@(MB@ST)	96 ± 8	100

[a] Measured from SEM images (100 nanoparticles); [b] MB retention from an aqueous solution at room temperature after 1 h (calculated from UV-vis analysis of the solution before and after being in contact with the nanoparticles). MB = methylene blue, u = uniform, cs = core–shell, csc = core–shell–corona, ST = stellate, RB = raspberry, r = radial, PhS = 2-phenylethylsilane.

2.2. Incorporation of Methylene Blue

In order to incorporate methylene blue into the silica nanoparticle, the surfactant was first removed from the as-made nanoparticle water suspensions. The drying step was circumvented in order to avoid particle aggregation. A treatment with ammonium nitrate in ethanol (96%) under sonication was used to remove the surfactant [31]. After three extraction cycles, the solvent was exchanged with water, using successive centrifugation steps.

The incorporation of methylene blue (MB) was then performed on aqueous surfactant-free samples. An n_{MB}:n_{SiO2} molar ratio of 0.00064 was adopted, as it was the highest ratio allowing only negligible MB leaching in our previously reported ST nanoparticles [32]. The incorporation of the photosensitizer was performed in water by stirring the mixture at

25 °C for 1 h. The resulting samples were named MB@u-ST, MB@u-RB, MB@cs-ST/RB, MB@cs-RB/r, and MB@csc-ST/PhS/RB, with u = uniform, cs = core–shell, and csc = core–shell–corona. The percentages of MB retained in the samples are reported in Table 1.

In addition, and in order to compare the above materials with a sample in which the MB is kept exclusively in the core of the particle, we tested the incorporation of MB into an ST nanoparticle followed by the addition of a layer of silica. Rougher nanoparticles were formed in these conditions, with RB external morphology (Figure 2f). We called this sample RB@(MB@ST).

2.3. Characterization of the Nanoparticles

2.3.1. Size Distribution and Colloidal Stability

A study of the colloidal stability was performed using dynamic light scattering (DLS). The samples were analyzed: (i) after the synthesis, that is, in the presence of the remaining surfactant; (ii) after surfactant extraction using NH_4NO_3 solution followed by several washings in water; and (iii) after further dilution of the previous surfactant-free colloidal suspension in water (Table S1). The u-ST nanoparticles present in the as-made supernatant were highly aggregated (average size ~800 nm). The surfactant acts as a glue, likely aggregating the particles. After extraction of the surfactant, no particle aggregation was discernable, and hydrodynamic diameters of around 200 nm were observed (aggregates of some particles). Upon further dilution in water (5 times) the particles were eventually separated (hydrodynamic diameters ~100 nm). On the contrary, the u-RB nanoparticles present in the as-made supernatant were more stable. A mean hydrodynamic particle diameter of ~120 nm was observed. Upon surfactant extraction and ultrasound treatment, the diameter slightly increased to ~185 nm (small aggregates likely generated by the ultrasound treatment).

The core–shell nanoparticles are quite stable, with hydrodynamic diameters close to the particle size, indicating the absence of large aggregates. For the core–shell–corona ST/PhS/RB nanoparticles, the same behavior as noted for the u-ST sample was observed: ~900 nm aggregates in the as-made sample that are disaggregated upon surfactant extraction.

The zeta potential was determined for the as-made u-ST and csc-ST/PhS/RB samples (Table S2). A value of −19 mV was observed for u-ST and −11 mV for csc-ST/PhS/RB, suggesting a surface more polar for u-ST than for csc-ST/PhS/RB. After surfactant extraction, the zeta-potential values shifted to −36 and −35 mV, respectively, indicating a higher colloidal stability. This is in agreement with the DLS observations. The absence of surfactant likely diminishes the trend of the particles towards aggregation.

2.3.2. Study of the Porosity of the Particles

Nitrogen sorption isotherms were performed for all the samples. Each type of nanoparticle morphology presents a specific profile of nitrogen sorption isotherm, as illustrated in Figure 3. The coincidence of the adsorption and desorption profiles indicates that there is no bottleneck effect and, therefore, no obstacle for desorption in the porous nanoparticles investigated here.

The absence of a neat step of adsorption near P/P_0~0.3 for the pure uniform stellate morphology (u-ST, Figure 3a) characterizes its specific open pores, [27] a determination which is consistent with the TEM images (see above). The conical shape of the pores produces progressive capillary condensation, starting with the filling of the narrow bottom of the cone at P/P_0~0.3 and ending with the wider side of the conical pores (ca. 15 nm), for an increasing committed volume at P/P_0~0.7. There is a rather low nitrogen absorption at low pressure, followed by an increasingly strong, or even very abrupt, absorption towards the end of pore filling, preceding capillary condensation in the interparticle volume above P/P_0~0.9. The shape of the curve is clearly not adapted to the determination of the pore volume from the t-plot. By contrast, the nitrogen isotherm of sample u-RB presents a neat adsorption step at P/P_0~0.35, followed by a flat plateau consistent with+, and pore sizes

defined by the narrow distribution typical of the RB morphology (Figure 3b). The nitrogen uptake above P/P_0~0.9 is slightly shifted to higher pressure compared to that of the u-ST sample, revealing larger interparticle voids and a lower packing compacity. For the u-ST sample, only the total surface can be calculated, namely, 361 $m^2 \cdot g^{-1}$ (Table 2). However, for the u-RB topology both internal and external surfaces can be deduced from the isotherm S_{int} = 244 $m^2 \cdot g^{-1}$ and S_{ext} = 126 $m^2 \cdot g^{-1}$.

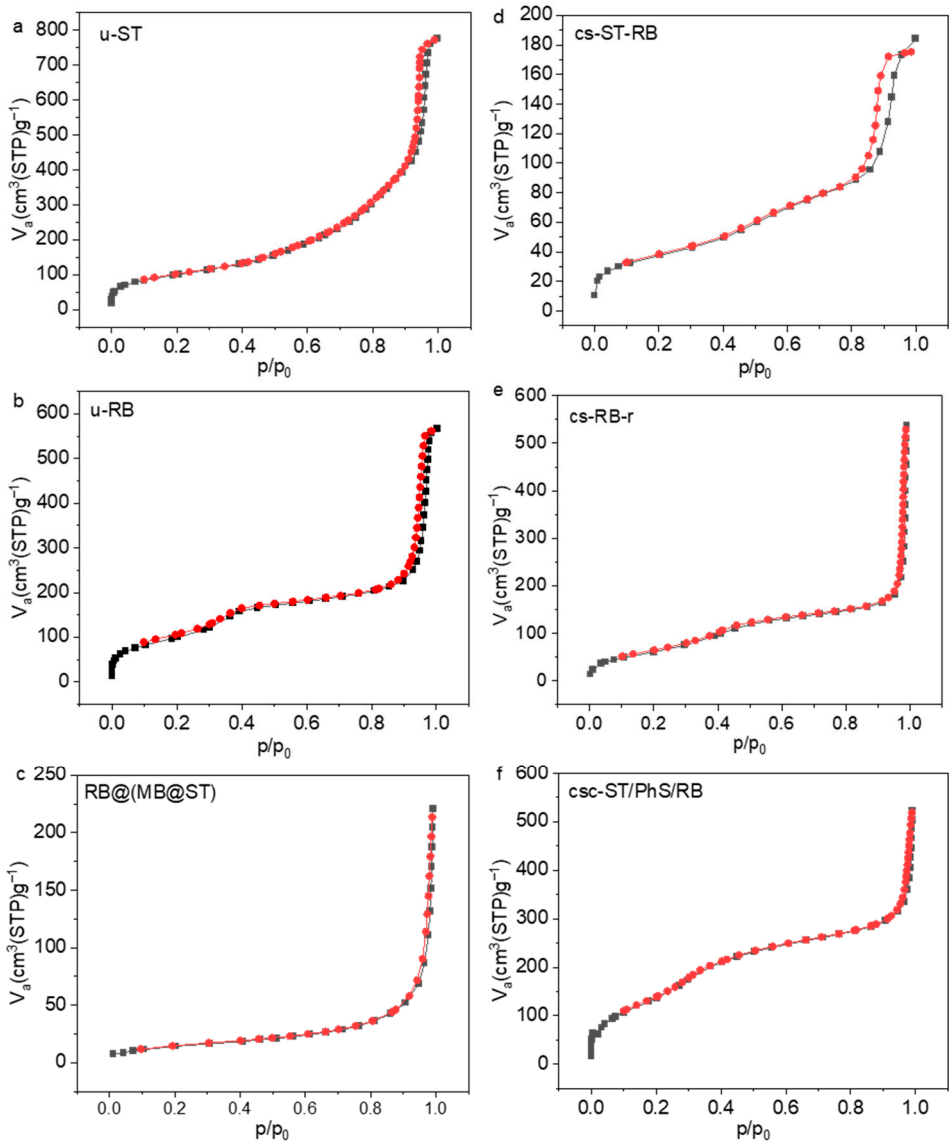

Figure 3. Nitrogen sorption isotherms at 77 K of samples (**a**) u-ST, (**b**) u-RB, (**c**) RB@(MB@ST), (**d**) cs-ST/RB, (**e**) cs-RB/r, and (**f**) csc-ST/PhS/RB. MB = methylene blue, u = uniform, cs = core–shell, csc = core–shell–corona, ST = stellate, RB = raspberry, r = radial, PhS = 2-phenylethylsilane. Black line = nitrogen adsorption, red line = nitrogen desorption.

In addition to these contrasting examples, there is another one that is particularly interesting, namely, the csc-ST/PhS/RB, which exhibits an isotherm profile containing a well-defined step of adsorption at P/P_0~0.3 which is consistent with single micelle templated pores, as expected for a pure RB morphology (Figure 3f). The corresponding pore volume accumulated at P/P_0~0.4 is higher (V_{int} = 0.32 $cm^3 \cdot g^{-1}$, Table 2) than that of pure u-RB (V_{int} = 0.19 $cm^3 \cdot g^{-1}$). This is surprising, since we were expecting the RB pore array only at the corona of the particle. After this adsorption step, the shape of the isotherm between P/P_0~0.5 and P/P_0~0.9 (Figure 3f) is not typical of conical pores

(Figure 3a), though the slope is more pronounced that than that of the pure RB. One may rationalize this information by assuming a reconstruction of the stellate core, which would tend towards another type of morphology. The specific surface of this sample is the largest of the series (S_{int} = 536 $m^2 \cdot g^{-1}$ and S_{ext} = 102 $m^2 \cdot g^{-1}$), suggesting a shift towards wormlike porosity [27,33].

Table 2. Porosity parameters deduced from the nitrogen sorption isotherms measured at 77 K (Figure 3).

Sample [a]	S_{tot} [b] ($m^2 \cdot g^{-1}$)	S_{ext} [c] ($m^2 \cdot g^{-1}$)	S_{int} [d] ($m^2 \cdot g^{-1}$)	V_{int} [e] ($cm^3 \cdot g^{-1}$)	$Ø_{BJH}$ [f] (nm)	$Ø_{ipv}$ [g] (nm)
u-ST	361	n.a. [h]	n.a. [h]	n.a. [h]	~3–15 nm	~42
u-RB	370	126	244	0.19	2.72	~50
cs-RB/r	276	68	208	0.16	3.2	>400
cs-ST/RB	131	78	53	0.059	3.2	~42
csc-ST/PhS/RB	638	102	536	0.32	2.5	>500
RB@(MB@ST)	66	~71	~0	n.a. [h]	n.a. [h]	>500

[a] named according to the Shape–Topology–Pore–Array nomenclature, SToPA (see text); [b] total surface area deduced from t-plot; [c] external surface area deduced from t-plot; [d] internal surface area calculated as $S_{int} = S_{tot} - S_{ext}$; [e] internal pore volume deduced from t-plot (Figure S4); [f] average pore diameter deduced from BJH (Figure S5); [g] interparticle packing void average size calculated from BJH model, and assuming a spherical shape; [h] n.a.: not accessible from the nitrogen sorption isotherms (see text).

The cs-ST/RB presents a sorption profile close to that of pure RB, with much less volume involved in the flat plateau (V_{int} = 0.059 $cm^3 \cdot g^{-1}$). This is consistent with the much smaller volume involved in the shell as compared to that of a nanoparticle presenting such uniform morphology in the whole of its internal volume. In addition, the lack of slope for the plateau indicates that the internal conical pores are not accessible, due to pore plugging. In comparison, the cs-RB/r sample exhibits the characteristics of large pores, with a plateau showing an obvious slope, though one starting late (adsorption step is above P/P_0~0.7). This might evidence the occurrence of truncated cones, as expected for radial centered pores in the corona region. The small volume engaged in this process (V_{int} = 0.16 $cm^3 \cdot g^{-1}$) is also consistent with the plugging of the interface between both morphologies. Another contrasting profile is provided by the RB@(MB@ST) sample, in which there is no detectable adsorption below P/P_0~0.9, which is consistent with a pore plugging effect, presumably due to the presence of MB molecules (Figure 3c).

In conclusion, our single-step synthesis of uniform stellate and raspberry porous nanoparticles was successfully achieved and yielded the expected pore characteristics. If a second growth step is carried out to generate a shell with a different pore morphology, the porosity of the core is rendered inaccessible. This is probably due to a plugging of the pores at the interface of the two morphologies. Surprisingly, developing an intermediate porous corona containing a hydrophobic silane additive prevents the plugging of the pores, thus making the porosity of the core accessible. Nonetheless, the core still undergoes partial pore morphology reconstruction, as can be inferred from the analysis of the nitrogen isotherm profiles.

2.3.3. UV-Visible Studies

The electronic spectrum of methylene blue (MB) in water displays the typical trace of its monomeric form only in dilute solutions, as described in the literature [34,35]. The spectrum presents a narrow band at around 660 nm, together with a vibronic shoulder at lower wavelength. At higher concentrations (typically above 10^{-6} M), the previously mentioned aggregation process takes place, and the formation of the dimeric form is evidenced by the appearance of a new band at around 605 nm.

We recorded UV-visible spectra in water suspension for the different samples containing MB in order to monitor the aggregation state in each case (Figure 4). As can be observed, for most of the samples, the monomer is the main form, present together with a

minor amount of the dimer. Then, an efficient distribution of the chromophore and thus the isolation of the photosensitizing species within the nanoparticle pores can be witnessed. An estimation of the percent of dimer present in each sample has been carried out by considering the contribution of both forms to the overall absorbance at 605 and 664 nm [35] (see Table S3, Supporting Information), yielding, in most cases, amounts of dimer below 14%. In particular, the incorporation of phenyl functions in MB@csc-ST/PhS/RB indeed reduces the dimer-to-monomer ratio, as the normalized absorbance at 605 nm is lower than that of the analogous MB@cs-ST/RB sample and the estimated percent of dimer drops from 13.7% to 9.3% upon phenyl incorporation.

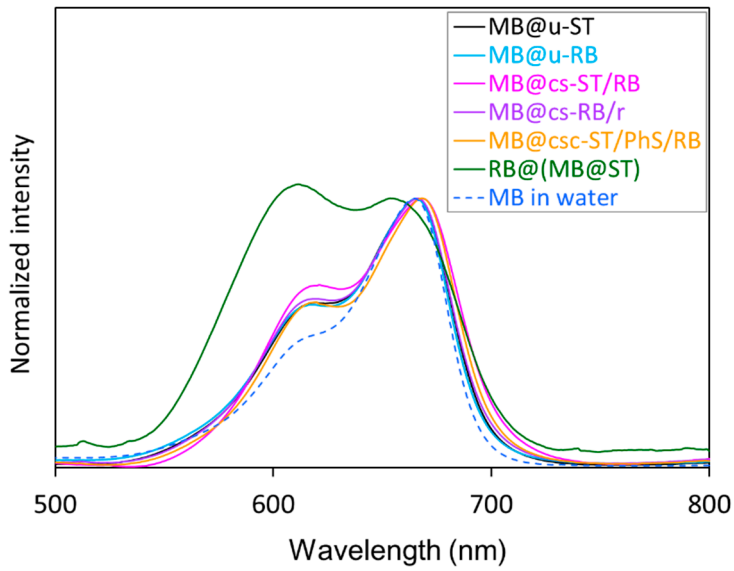

Figure 4. UV-visible spectra in water of MB@u-ST, MB@u-RB, MB@cs-ST/RB, MB@cs-RB/r, MB@csc-ST/PhS/RB, and RB@(MB@ST) samples, together with the UV-vis spectrum of MB in diluted aqueous solution (dashed line). MB = methylene blue, u = uniform, cs = core–shell, csc = core–shell–corona, ST = stellate, RB = raspberry, r = radial, PhS = 2-phenylethylsilane.

Among the series, a notable exception is seen for the case of RB@(MB@ST), in which a significant contribution of the dimeric form (estimated to be higher than 39%) is observed. This outstanding unique MB dimerization process could be consistent with a higher pH during the growth of the RB shell on the top of the MB@ST particles (pH~8.5). In addition, there is a slight hypsochromic shift in this sample for the band corresponding to the monomer form, with a maximum wavelength close to that displayed by MB monomer in organic solvents [36,37]. This would suggest a decrease in polarity in the MB environment, which arises from the more restricted access of water to the MB molecules. Nevertheless, the low MB dimer ratio found for most of the samples, in sharp contrast with the tendency to aggregation described when MB is incorporated in solid supports [12,38,39], is remarkable.

2.4. Singlet Oxygen Generation

We carried out $^1O_2$ generation experiments for all the samples displaying complete MB retention (MB@u-ST, MB@cs-ST/RB, MB@csc-ST/PhS/RB, and RB@(MB@ST)), in both water and methanol suspensions, in order to compare their performance with that of free MB and also with those of our previous systems based on a stellate type of nanoparticles [32]. We monitored the photobleaching of ADPA (3,3′-(anthracene-9,10-diyl) dipropanoic acid) used as an $^1O_2$ scavenging probe, using the decrease of its characteristic fluorescence signal as outlined in our previously reported methodology, here described in Section 3. By doing so, we avoid the artefacts typically obtained using UV-vis absorption monitoring, such as the formation of absorbing photodegradation products [40]. The concentration of ADPA in the samples was constant in all experiments (solution being prepared from concentrated

stock solution of the latter), while concentrations of photosensitizing species were adjusted to obtain equal absorbance at the irradiation wavelength used throughout all monitoring experiments (629 nm, see the experimental section for details).

2.4.1. Studies in Water

The evolution of the ADPA luminescence intensity in water suspension follows a first-order kinetics for all the samples, as well as for the MB aqueous solution (Figure 5). The MB-functionalized nanoparticles display photocatalytic activity, though it is in all cases lower than that shown by free MB, presumably due to slow kinetics for in-and-out triplet/singlet oxygen diffusion through the matrix mesopores. This would be consistent with the higher performance observed for MB@csc-ST/PhS/RB, as it is the sample with the larger porous volume (see Figure 3 and Table 2), and this presumably allows for an increased diffusion rate. Also, for this sample, the phenyl functions led to a smaller ratio of dimerized MB, consequently minimizing aggregation-related deactivation mechanisms.

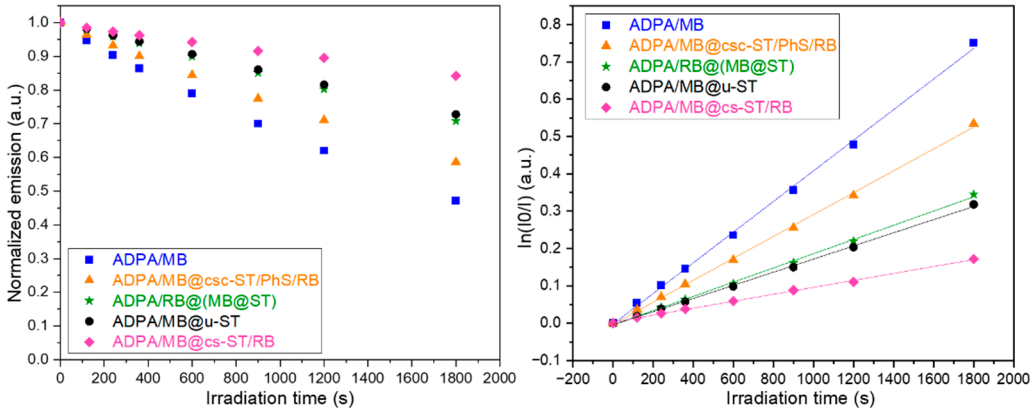

Figure 5. First-order plot of the evolution in ADPA luminescence vs. irradiation time for all the samples studied in water (irradiation wavelength = 629 nm; ADPA luminescence registered at 409 nm after excitation at 358 nm).

Sample MB@cs-ST/RB is the one with least photosensitizing ability, which could be in part explained by its small porous volume, together with its irregular external surface, one which could involve the occurrence of a wide diversity of pore diameters, in some cases of very small size. On the other hand, samples MB@u-ST and RB@(MB@ST) show surprisingly close performance despite their different MB aggregation states, topologies, and pore morphologies. At a first glance, the addition of a final RB shell in RB@(MB@ST) seems not to have had a significant influence on $^1O_2$ generation ability. We can, however, not exclude at this stage that mid-term stability studies could reveal roles still unidentified in the present studies, such as extra protection against MB leaching.

2.4.2. Studies in Methanol

Singlet oxygen monitoring in methanol as a solvent reveals a slightly improved activity (around 7% higher) for free MB compared to the measures carried out in water, whereas the photocatalytic activity of the nanoparticle samples is increased in the range of 50% to 100%, while the same relative activity among nanoparticle-based systems as that displayed in water is maintained (see Figures S6 and S7). This behavior clearly manifests the matrix effect in the diffusion of molecular species, together with the well-known influence of the solvent in the $^1O_2$ lifetime and the singlet-to-triplet deactivation through non radiative processes, which is more significant for solvents presenting a high proticity, and thus stronger in water than in methanol [41]. We assume that this effect is particularly marked in the NP-based PS, since it is essential in these systems that the $^1O_2$ escapes the pores of the NP in order to enable reaction with ADPA, making lifetime of the excited species a highly critical factor in the overall reactivity of the system. The nanoparticle-based samples described in this

work display slightly more moderate activity when methanol is used as a solvent, when compared to our previously reported ST-based systems [32]. Nevertheless, in the latter case the nanoparticles were isolated in a solid state and once re-suspended, the corresponding solutions exhibited limited stability and formed aggregates when the samples were left unstirred, thus precluding their use in clinical applications such as PDT. The colloidal MB-functionalized nanoparticles described here combine extensive control of the topology and pore morphology with an outstanding stability in aqueous suspension and an activity in singlet oxygen generation that remains high in spite of our abovementioned determination.

2.5. Theoretical Description of the Monomeric and Dimeric Structures

To provide a molecular insight into the aggregation of MB units, Density Functional Theory (DFT) calculations were performed. The MB exhibits a rather ionic structure, with a S-Cl bond distance of 2.586 Å, and, notably, a N-S-Cl angle of 116.9° (see Figure 6a). Actually, the Mayer Bond Order (MBO) for the S···Cl interaction is only 0.323, and thus confirms its ionic character, being a clearly lower value than the 1.115 MBO computed for both covalent S-C bonds of the molecule [42]. The π-π stacking interaction of two units (Figure 6b) is favored up to 21.4 kcal/mol with regard to the monomeric form. Hence, while the π-π stacking effect may seem crucial [43], configuring the two MB units in a quasi-planar manner achieves a conformation only 0.7 kcal/mol above, forming an almost rhombic S_2Cl_2 core between the two units (Figure 6c). This prompted us to evaluate the combination of both effects under a tetrameric aggregate, resulting in a synergistic stabilization of up to 48.4 kcal/mol. Tetrameric units of MB are assumed to be significantly present in solution only at relatively high MB concentrations (above 10^{-4} M) [34]. However, the aggregate structure has not been precisely determined, and it is assumed to be built from π-stacked MB units, with an uncertain role played by chloride counterions. In this layout, the four units are not parallel; rather, they are arranged in two pairs of parallel planes, and the chlorines simply enhance the interaction of non-parallel units, as depicted in Figure 6d.

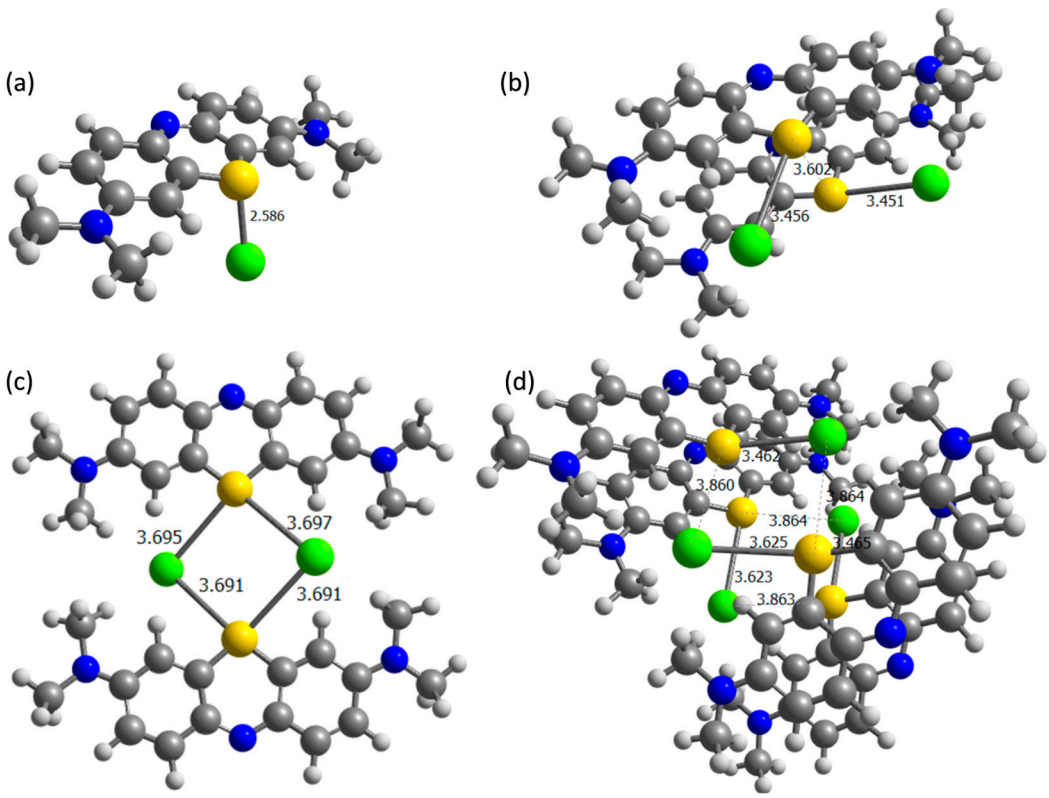

Figure 6. DFT-computed structures of the (**a**) monomer, (**b**) stacked dimer, (**c**) planar dimer, and (**d**) tetramer of MB (selected distances in Å). Yellow = S, green = Cl, and blue = N.

To assess the effect of the halide in the monomer, a similar calculation was made in the absence of the anion, revealing surprisingly increased stability values of 17.4 kcal/mol and 14.1 kcal/mol in the monomer and dimer forms, respectively. Thus, separating the cationic part results in enhanced stability. A similar effect is found experimentally by Marbán et al. for tetrameric aggregates through mathematical fitting of UV-vis spectra [34]. The addition of the organic 2-phenylethylsilane (PhS) moiety was also explored, and it was found to stabilize the monomer by 3.2 kcal/mol, which would explain the lower occurrence of the dimeric form evidenced by UV-vis spectra of the phenyl-functionalized MB@csc-ST/PhS/RB sample when compared to the analogous MB@cs-ST/RB. Furthermore, although all calculations were performed with water as the implicit solvent, its explicit effect was also considered. Water exhibits a slightly higher stabilization effect compared to PhS, reaching 4.3 kcal/mol. For dimers, whether stacked or in the same plane, there is a negligible stabilization of 0.3 kcal/mol, and an even destabilization of 3.6 kcal/mol, respectively. Thus, the effect of water, or, by extension, silane, competes with the aggregation of monomeric units.

In an attempt to rationalize the experimental UV-vis spectra obtained (Figure 4), time-dependent DFT studies were conducted. In all cases, above 300 nm, only one band with significant intensity was observed. For the monomer, this band appeared prominently at 485.0 nm, while for the dimer, it occurred at 522.8 nm. This seems to be out of sync with the experimental results. However, upon adding one or two water molecules, the results showed a bathochromic shift. For the monomer, the peak shifted to 527.3 nm, whereas for the dimer, it became hypsochromic, reaching 511.8 nm. In the case in which the dimer structure was not stacked, the peak shifted even further, to 509.1 nm. Conversely, in the case of the monomer with PhS, there was a bathochromic effect, shifting the peak to 550.0 nm. Additional calculations, excluding the halides, revealed that they were not relevant, as the computed structures showed nearly identical values.

3. Materials and Methods

Methylene blue trihydrate (MB, 98%) and tetraethyl orthosilicate (TEOS, 99%) were purchased from Alfa Aesar (Haverhill, MA, USA). Hexadecyltrimethylammonium p-toluenesulfonate (CTATos, 98%), triethanolamine ($TEAH_3$, 99%), and 3,3′-(anthracene-9,10-diyl) dipropanoic acid (ADPA, 97%) were purchased from Sigma-Aldrich (Saint-Louis, MO, USA). Hexadecyl trimethyl ammonium bromide (CTABr, 99%) was purchased from Thermofisher. 2-phenylethyltrimethoxysilane (97%) was purchased from ABCR (Karlsruhe, Germany)). Ethanol (96%) and methanol (99.9%) were purchased from Carlo Erba (Milano, Italia). All of the chemicals and solvents were used as received.

3.1. Syntheses of the Materials

All of the silica nanoparticles were synthesized by mechanical stirring. The samples were not dried and were continuously maintained in a water suspension.

3.1.1. Uniform Stellate Silica Nanoparticles (u-ST)

The stellate silica nanoparticles were prepared according to the description of Zhang et al., with some modifications [27]. CTATos (1.66 g, 3.64 mmol) and triethanolamine ($TEAH_3$, 0.30 g, 2.01 mmol) were added to 100 mL of water, and the solution was stirred and heated to 80 °C. After 1 h, 14 mL of TEOS (62.77 mmol) was added to the solution. The stirring rate during synthesis was kept at 500 rpm. The mixture was heated for 2 h at 80 °C. This corresponds to a solution of around 30 $g \cdot L^{-1}$ in silica.

3.1.2. Uniform Raspberry Silica Nanoparticles (u-RB)

The raspberry silica nanoparticles were prepared according to the description of Zhang et al., with some modifications [27]. CTABr (1.33 g, 3.64 mmol) and triethanolamine ($TEAH_3$, 0.30 g, 2.01 mmol) were added to 100 mL of water, and the solution was heated to

80 °C while being stirred at 200 rpm. After 1 h, 14 mL of TEOS (62.77 mmol) was added to the solution and it was stirred at 100 rpm overnight.

3.1.3. Core–Shell–Corona csc-ST/PhS/RB

The synthesis was similar to the procedure used to synthesize u-ST nanoparticles. CTATos (1.66 g, 3.64 mmol) and triethanolamine ($TEAH_3$, 0.30 g, 2.01 mmol) were added to 100 mL of water and the solution was stirred mechanically (500 rpm) and heated to 80 °C. After 1 h, 14 mL of TEOS (62.77 mmol) was added to the solution and the mixture was first stirred at 500 rpm for 15 min and then at stirred at 100 rpm for 45 min. After that, 0.14 mL of 2-phenylethyltrimethoxysilane (0.64 mmol) was added, and the solution was stirred at 100 rpm for 1 h. In the end, 2.8 mL TEOS (12.55 mmol) was added to the mixture, which was then stirred at 100 rpm for another 1 h.

3.1.4. Core–Shell cs-ST/RB

The u-ST nanoparticles were prepared as described above. Then, to half of the u-ST silica nanoparticle solution, CTABr (0.67 g, 1.82 mmol), triethanolamine ($TEAH_3$, 0.15 g, 1.05 mmol) and 50 mL of water were added, and the mixture was stirred at 80 °C for 1 h. In the end, 7 mL of TEOS (31.4 mmol) was added, and the mixture was further heated for 2 h at 80 °C.

3.1.5. Core–Shell cs-RB/r

The u-RB nanoparticles were prepared as described earlier. Then, to half of the u-RB silica nanoparticle solution, CTATos (0.83 g, 1.82 mmol), triethanolamine ($TEAH_3$, 0.15 g, 1.05 mmol) and 50 mL of water were added. The mixture was stirred at 80 °C for 1 h. In the end, 7 mL of TEOS (31.38 mmol) was added and the mixture was further heated for 2 h at 80 °C.

3.2. Extraction of the Surfactant Using NH_4NO_3 as Washing Reagent

The surfactants of all the samples were extracted by three washings of 30 min each in an ethanolic solution of ammonium nitrate at 6 $g \cdot L^{-1}$ using an ultrasonic bath. The nanoparticles were then washed three times with water.

3.3. Incorporation of MB

The required volumes of u-ST, u-RB, csc-ST/PhS/RB, cs-ST/RB, and cs-RB/r solutions (after removal of the surfactants) were added into five different Erlenmeyer flasks, each containing 2 mg of methylene blue trihydrate, to achieve an n_{MB}:n_{SiO2} molar ratio of 0.00064. The volume of each solution was brought to 25 mL by the addition of water and the mixtures were stirred at 25 °C for 1 h. The resulting samples were, respectively, named MB@u-ST, MB@u-RB, MB@csc-ST/PhS/RB, MB@cs-ST/RB, and MB@cs-RB/r.

3.4. Synthesis of RB@(MB@ST)

The required volume of u-ST suspension, prior to the extraction of the surfactant, was added into an Erlenmeyer flask containing 2 mg of methylene blue trihydrate, to achieve an n_{MB}:n_{SiO2} molar ratio of 0.00064. Water was added in order to reach a final volume of 25 mL. The mixture was stirred at 25 °C for 1 h to obtain the MB@u-ST solution. Then, CTABr (0.133 g, 0.36 mmol), triethanolamine ($TEAH_3$, 0.030 g, 0.20 mmol), and 10 mL water were added to MB@u-ST solution and the mixture was stirred mechanically at 500 rpm and heated to 80 °C. After 1 h, 1.4 mL of TEOS was added to the solution and it was stirred at 500 rpm for 2 h. The extraction of surfactant was carried out at the end by following the process mentioned above.

3.5. Characterization of the Samples

Nitrogen sorption isotherms at 77 K were performed with a Belsorp Max volume device on solids that were dried under vacuum overnight at 80 °C. Solid-state UV-visible

spectra determinations were performed on samples diluted with calcined silica in a Jasco V-770 spectrometer. UV-visible spectra in solution were recorded using a Jasco V-730 spectrometer. Dynamic light scattering (DLS) measurements were carried out on suspensions with silica concentration levels of around 1 $g \cdot L^{-1}$ using a Cordouan DL 135 particle-size analyzer instrument. SEM images were recorded using a JEOL JSM-IT800 electronic microscope, examining solid samples deposited on a copper tape. Transmission electron microscopy (TEM) images were performed using a JEOL 1200 EXII microscope. Samples for TEM measurements were deposited from suspensions on copper grids and allowed to dry before observation.

3.6. Luminescence Studies and Singlet Oxygen Generation

Luminescence spectra were recorded using a Horiba-Jobin-Yvon Fluorolog-3® spectrofluorometer equipped with a three-slit double-grating excitation and emission monochromator, with dispersions of 2.1 $nm \cdot mm^{-1}$ (1200 $grooves \cdot mm^{-1}$). An R928 detector was used for emission-intensity measurements in the visible range [400–845 nm]. Spectra were reference-corrected for the emission spectral response (detector and grating). In order to study the $^1O_2$ generation efficiency using 3,3′-(anthracene-9,10-diyl)dipropanoic acid (ADPA) as a scavenger, 2 mL of freshly prepared solutions of ADPA and the sample to be studied were placed in a three mL open quartz cuvette (1 × 1 × 3 cm), and stirred at 100 rpm for the whole irradiation period. The initial optical density of ADPA in the reaction mixture was 0.3 at the irradiation wavelength, which was centered at 358 nm.

All of the samples were adjusted in concentration so that the initial absorbance of the MB photosensitizer at 629 nm was similar in all cases (OD ca 0.15). Samples were then irradiated over given periods of time using a spectrofluorometer xenon arc lamp as an irradiation source. The irradiation wavelength was centered at 629 nm, and entrance slit openings were set to 10 nm. This setup ensured constant irradiation power throughout all the irradiation experiments.

Conversion of the ADPA scavenger upon reaction with the photogenerated oxygen was followed by regular measurements of the luminescence signal of the latter (considering it to be linearly proportional to its concentration, which is valid in the investigated range of absorbance, with OD of 0.1), consecutive to the excitation performed at 358 nm. The plot of the ADPA concentration decay was determined using a luminescence intensity of 409 nm.

3.7. Computational Details

The DFT calculations were performed using the Gaussian16 suite of programs [44]. The molecular systems' electronic configurations were described using the hybrid GGA functional developed by Becke and Lee, Yang, and Parr [45–47], with the dispersion corrections accounted for using the D3 Grimme scheme method (GD3 keyword in Gaussian) [48], and employing the Ahlrichs basis set def2SVP [49,50]. Geometry optimizations were carried out without symmetry constraints, and the characterizations of local stationary points were achieved through analytical frequency calculations. These frequencies were utilized to compute unscaled zero-point energies (ZPEs), as well as thermal corrections and entropy effects at 298.15 K. Computed UV-Vis spectra were generated via single-point energy calculations using the CAM-B3LYP-D3 functional and the def2TZVP basis set. Solvent effects were incorporated using the Solvation Model based on Density (SMD) [51], with water employed as the solvent.

4. Conclusions

In summary, in this study we have shown that it is possible to control the internal pore morphology and topology of a silica nanoparticle by modifying some of the synthesis parameters, such as the counter-ion of the surfactant which generates the porosity, and the amount and nature of the base used to control the pH. In addition, both the time and the speed of the stirring during the synthesis of the silica nanoparticles have an effect on the final size of the particles. Furthermore, the organic modification of the internal surface

for the retention of a targeted molecule is a delicate issue that greatly depends on the experimental conditions, and influences both the topologies and the morphologies of the nanoparticles. These are key issues in ascertaining the amount, aggregation, and activity of the hosted molecule.

Here, we have focused on the incorporation of methylene blue (MB) in porous silica nanoparticles and its retention, playing with the porous morphology and targeting the presence of phenyl functions located close to the exterior of the particles. We have shown that the topology and porous morphology of the silica matrix influences the singlet oxygen generation of the hosted MB. In particular, the highest catalytic activity is obtained with the core–shell–corona csc-ST/PhS/RB sample. This approach could be applied, not only to other hydrophilic photosensitizers and active molecules, but also to hydrophobic ones, by adapting the hosting nanoparticle's internal characteristics.

Supplementary Materials: The following supporting information can be downloaded at: https://www.mdpi.com/article/10.3390/inorganics12060155/s1, Figure S1: TEM images of u-RB nanoparticles 5 weeks after the synthesis; Figure S2: SEM images of u-RB nanoparticles 5 weeks after the synthesis; Figure S3: SEM images of 45 nm particles with phenyl moieties. Figure S4: t-plot of nitrogen sorption isotherms measurements; Figure S5: BJH analysis of nitrogen sorption isotherms measurements; Figure S6: First-order plot of the evolution in ADPA luminescence vs. irradiation time for all the samples studied in methanol suspension; Figure S7: First-order plot of the evolution in ADPA luminescence vs. irradiation time for pure MB with ADPA and MB@cs-ST/RB samples in water and methanol; Figure S8: DFT-computed structures. Table S1: Size analyses from DLS and comparison with the size deduced from SEM and TEM images; Table S2: Zeta-potential measurements; Table S3: Estimated values of dimer ratio inferred from UV-vis spectra; Table S4: xyz coordinates and absolute energies (in a.u.) of all computed DFT species.

Author Contributions: Conceptualization, L.B., M.R.-P. and B.A.; methodology, J.X., C.M., L.B., K.Z., Y.G., M.R.-P., A.P. and B.A.; validation, J.X., C.M., L.B., M.R.-P. and B.A.; formal analysis, J.X.; investigation, J.X. and A.P.; resources, C.M., L.B., A.P., Y.G. and B.A.; data curation, J.X., C.M., L.B., M.R.-P. and B.A.; writing—original draft preparation, J.X., L.B., A.P., M.R.-P. and B.A.; writing—review and editing, C.M., Y.G., L.B., A.P., M.R.-P. and B.A.; visualization, J.X., L.B., M.R.-P. and B.A.; supervision, L.B., M.R.-P. and B.A.; project administration, L.B., A.P. and B.A.; funding acquisition, L.B. and B.A. All authors have read and agreed to the published version of the manuscript.

Funding: This research was funded by CNRS UMR-5182 and the Ecole Normale Supérieure de Lyon; the Spanish MINECO, for project PID2021-127423NB-I00; and the Generalitat de Catalunya, for project 2021SGR623.

Data Availability Statement: The raw data supporting the conclusions of this article will be made available by the authors on request.

Acknowledgments: J.X. greatly acknowledges the China Scholarship Council for PhD scholarship. A.P. is a Serra Húnter Fellow, and holder of the ICREA Academia Prize 2019. The Research Writing Workshop of the Centre de Langues de l'Ecole Normale, Superiéure de Lyon, and especially Layla Roesler, is also acknowledged for their help in improving the manuscript.

Conflicts of Interest: The authors declare no conflicts of interest.

Abbreviations

ADPA: 3,3′-(anthracene-9,10-diyl)dipropanoic acid; cs: core–shell; csc: core–shell–corona; CTATos: hexadecyltrimethylammonium p-toluenesulfonate; DFT: Density Functional Theory; DLS: diffusion light scattering; IR: infrared; r: radial; OD: optical density; RB: raspberry; SEM: scanning electron microscopy; ST: stellate; SToPA: shape-topology-pore-array; TEOS: tetraethyl orthosilicate; $TEAH_3$: triethanolamine; TEM: transmission electron microscopy; UV: ultraviolet.

References

1. Bray, F.; Laversanne, M.; Sung, H.; Ferlay, J.; Siegel, R.L.; Soerjomataram, I.; Jemal, A. Global Cancer Statistics 2022: GLOBOCAN Estimates of Incidence and Mortality Worldwide for 36 Cancers in 185 Countries. *CA Cancer J. Clin.* **2024**, *74*, 229–263. [CrossRef] [PubMed]
2. Markham, M.J.; Wachter, K.; Agarwal, N.; Bertagnolli, M.M.; Chang, S.M.; Dale, W.; Diefenbach, C.S.M.; Rodriguez-Galindo, C.; George, D.J.; Gilligan, T.D.; et al. Clinical Cancer Advances 2020: Annual Report on Progress against Cancer from the American Society of Clinical Oncology. *J. Clin. Oncol.* **2020**, *38*, 1081–1101. [CrossRef] [PubMed]
3. Lucky, S.S.; Soo, K.C.; Zhang, Y. Nanoparticles in photodynamic therapy. *Chem. Rev.* **2015**, *115*, 1990–2042. [CrossRef] [PubMed]
4. Foote, C.S. Definition of type I and type II photosensitized oxidation. *Photochem. Photobiol.* **1991**, *54*, 659. [CrossRef] [PubMed]
5. Baptista, M.S.; Cadet, J.; Di Mascio, P.; Ghogare, A.A.; Greer, A.; Hamblin, M.R.; Lorente, C.; Nunez, S.C.; Ribeiro, M.S.; Thomas, A.H.; et al. Type I and Type II Photosensitized Oxidation Reactions: Guidelines and Mechanistic Pathways. *Photochem. Photobiol.* **2017**, *93*, 912–919. [CrossRef] [PubMed]
6. Zhao, X.; Liu, J.; Fan, J.; Chao, H.; Peng, X. Recent progress in photosensitizers for overcoming the challenges of photodynamic therapy: From molecular design to application. *Chem. Soc. Rev.* **2021**, *50*, 4185–4219. [CrossRef]
7. Li, X.; Kwon, N.; Guo, T.; Liu, Z.; Yoon, J. Innovative Strategies for Hypoxic-Tumor Photodynamic Therapy. *Angew. Chem. Int. Ed.* **2018**, *57*, 11522–11531. [CrossRef] [PubMed]
8. Chilakamarthi, U.; Giribabu, L. Photodynamic Therapy: Past, Present and Future. *Chem. Record* **2017**, *17*, 775–802. [CrossRef] [PubMed]
9. Redmond, R.W.; Gamlin, J.N. A compilation of singlet oxygen yields from biologically relevant molecules. *Photochem. Photobiol.* **1999**, *70*, 391–475. [CrossRef] [PubMed]
10. Oz, M.; Lorke, D.E.; Hasan, M.; Petroianu, G.A. Cellular and molecular actions of Methylene Blue in the nervous system. *Med. Res. Rev.* **2011**, *31*, 93–117. [CrossRef] [PubMed]
11. Tardivo, J.P.; Del Giglio, A.; de Oliveira, C.S.; Gabrielli, D.S.; Junqueira, H.C.; Tada, D.B.; Severino, D.; de Fatima Turchiello, R.; Baptista, M.S. Methylene blue in photodynamic therapy: From basic mechanisms to clinical applications. *Photodiagnosis Photodyn. Ther.* **2005**, *2*, 175–191. [CrossRef] [PubMed]
12. Severino, D.; Junqueira, H.C.; Gugliotti, M.; Gabrielli, D.S.; Baptista, M.S. Influence of Negatively Charged Interfaces on the Ground and Excited State Properties of Methylene Blue. *Photochem. Photobiol.* **2003**, *77*, 459–468. [CrossRef] [PubMed]
13. DeRosa, M.C.; Crutchley, R.J. Photosensitized singlet oxygen and its applications. *Coord. Chem. Rev.* **2002**, *233–234*, 351–371. [CrossRef]
14. Sass, M.D.; Caruso, C.J.; Axelrod, D.R. Accumulation of methylene blue by metabolizing erythrocytes. *J. Lab. Clin. Med.* **1967**, *69*, 447–455. [PubMed]
15. Bongard, R.D.; Merker, M.P.; Shundo, R.; Okamoto, Y.; Roerig, D.L.; Linehan, J.H.; Dawson, C.A. Reduction of thiazine dyes by bovine pulmonary arterial endothelial cells in culture. *Amer. J. Physiol.* **1995**, *269*, L78–L84. [CrossRef] [PubMed]
16. Olson, L.E.; Merker, M.P.; Patel, M.K.; Bongard, R.D.; Daum, J.M.; Johns, R.A.; Dawson, C.A. Cyanide increases reduction but decreases sequestration of methylene blue by endothelial cells. *Annals Biomed. Eng.* **2000**, *28*, 85–93. [CrossRef] [PubMed]
17. Gabrielli, D.; Belisle, E.; Severino, D.; Kowaltowski, A.J.; Baptista, M.S. Binding, aggregation and photochemical properties of methylene blue in mitochondrial suspensions. *Photochem. Photobiol.* **2004**, *79*, 227–232. [CrossRef]
18. Wagner, S.J.; Skripchenko, A.; Robinette, D.; Foley, J.W.; Cincotta, L. Factors affecting virus photoinactivation by a series of phenothiazine dyes. *Photochem. Photobiol.* **1998**, *67*, 343–349. [CrossRef] [PubMed]
19. Vallet-Regi, M.; Schuth, F.; Lozano, D.; Colilla, M.; Manzano, M. Engineering mesoporous silica nanoparticles for drug delivery: Where are we after two decades? *Chem. Soc. Rev.* **2022**, *51*, 5365–5451. [CrossRef]
20. Prieto-Montero, R.; Arbeloa, T.; Martinez-Martinez, V. Photosensitizer-Mesoporous Silica Nanoparticles Combination for Enhanced Photodynamic Therapy(dagger). *Photochem. Photobiol.* **2023**, *99*, 882–900. [CrossRef] [PubMed]
21. Lérida-Viso, A.; Estepa-Fernández, A.; García-Fernández, A.; Martí-Centelles, V.; Martínez-Máñez, R. Biosafety of mesoporous silica nanoparticles; towards clinical translation. *Adv. Drug Deliver. Rev.* **2023**, *201*, 115049. [CrossRef] [PubMed]
22. Xu, Q.; Yang, Y.; Lu, J.; Lin, Y.; Feng, S.; Luo, X.; Di, D.; Wang, S.; Zhao, Q. Recent trends of mesoporous silica-based nanoplatforms for nanodynamic therapies. *Coord. Chem. Rev.* **2022**, *469*, 214687. [CrossRef]
23. Makhadmeh, G.N.; Abdul Aziz, A.; Abdul Razak, K. The efficacy of methylene blue encapsulated in silica nanoparticles compared to naked methylene blue for photodynamic applications. *Artif. Cells Nanomed. Biotechnol.* **2016**, *44*, 1018–1022. [CrossRef] [PubMed]
24. Sun, J.; Fan, Y.; Zhang, P.; Zhang, X.; Zhou, Q.; Zhao, J.; Ren, L. Self-enriched mesoporous silica nanoparticle composite membrane with remarkable photodynamic antimicrobial performances. *J. Col. Inter. Sci.* **2020**, *559*, 197–205. [CrossRef] [PubMed]
25. Yang, Y.; Chen, F.; Xu, N.; Yao, Q.; Wang, R.; Xie, X.; Zhang, F.; He, Y.; Shao, D.; Dong, W.F.; et al. Red-light-triggered self-destructive mesoporous silica nanoparticles for cascade-amplifying chemo-photodynamic therapy favoring antitumor immune responses. *Biomaterials* **2022**, *281*, 121368. [CrossRef] [PubMed]
26. Seo, S.H.; Kim, B.M.; Joe, A.; Han, H.W.; Chen, X.; Cheng, Z.; Jang, E.S. NIR-light-induced surface-enhanced Raman scattering for detection and photothermal/photodynamic therapy of cancer cells using methylene blue-embedded gold nanorod@SiO_2 nanocomposites. *Biomaterials* **2014**, *35*, 3309–3318. [CrossRef] [PubMed]

27. Zhang, K.; Xu, L.-L.; Jiang, J.-G.; Calin, N.; Lam, K.-F.; Zhang, S.-J.; Wu, H.-H.; Wu, G.-D.; Albela, B.; Bonneviot, L.; et al. Facile Large-Scale Synthesis of Monodisperse Mesoporous Silica Nanospheres with Tunable Pore Structure. *J. Amer. Chem. Soc.* **2013**, *135*, 2427–2430. [CrossRef] [PubMed]
28. Zhang, K.; Yang, T.Q.; Shan, B.Q.; Liu, P.C.; Peng, B.; Xue, Q.S.; Yuan, E.H.; Wu, P.; Albela, B.; Bonneviot, L. Dendritic and Core-Shell-Corona Mesoporous Sister Nanospheres from Polymer-Surfactant-Silica Self-Entanglement. *Chem. Eur. J.* **2018**, *24*, 478–486. [CrossRef] [PubMed]
29. de Souza, E.S.J.M.; Hanchuk, T.D.; Santos, M.I.; Kobarg, J.; Bajgelman, M.C.; Cardoso, M.B. Viral Inhibition Mechanism Mediated by Surface-Modified Silica Nanoparticles. *ACS Appl. Mater. Inter.* **2016**, *8*, 16564–16572. [CrossRef] [PubMed]
30. Sadasivan, S.; Fowler, C.E.; Khushalani, D.; Mann, S. Nucleation of MCM-41 nanoparticles by internal reorganization of disordered and nematic-like silica surfactant clusters. *Angew. Chem. Int. Ed.* **2002**, *41*, 2151–2153. [CrossRef]
31. Pelluau, T.; Sene, S.; Garcia-Cirera, B.; Albela, B.; Bonneviot, L.; Larionova, J.; Guari, Y. Multifunctionalized Mesostructured Silica Nanoparticles Containing Mn2 Complex for Improved Catalase-Mimicking Activity in Water. *Nanomaterials* **2022**, *12*, 16. [CrossRef] [PubMed]
32. Xu, J.; Pelluau, T.; Guari, Y.; Bonneviot, L.; Rodríguez-Pizarro, M.; Albela, B. Incorporation of methylene blue into mesoporous silica nanoparticles for singlet oxygen generation. *New J. Chem.* **2023**, *47*, 1861–1871. [CrossRef]
33. Kobler, J.; Möller, K.; Bein, T. Colloidal suspensions of functionalized mesoporous silica nanoparticles. *ACS Nano* **2008**, *2*, 791–799. [CrossRef] [PubMed]
34. Fernández-Pérez, A.; Marbán, G. Visible Light Spectroscopic Analysis of Methylene Blue in Water; What Comes after Dimer? *ACS Omega* **2020**, *5*, 29801–29815. [CrossRef] [PubMed]
35. Florence, N.; Naorem, H. Dimerization of methylene blue in aqueous and mixed aqueous organic solvent: A spectroscopic study. *J. Mol. Liq.* **2014**, *198*, 255–258. [CrossRef]
36. Hemdan, S.S. The Shift in the Behavior of Methylene Blue toward the Sensitivity of Medium: Solvatochromism, Solvent Parameters, Regression Analysis and Investigation of Cosolvent on the Acidity Constants. *J. Fluoresc.* **2023**, *33*, 2489–2502. [CrossRef] [PubMed]
37. Leonardo Marmo, M.; Juliana Pereira, L.; Adriana, L.; Lúcia, C.; Divinomar, S.; Maurício da Silva, B.; André Luiz, T.; Adriana Passarela, G.; Noboru, H.; Maira Regina, R.; et al. The Methylene Blue Self-aggregation in Water/Organic Solvent Mixtures: Relationship between Solvatochromic Properties and Singlet Oxygen Production. *Orbital Elect. J. Chem.* **2017**, *9*, 279–289.
38. Saita, S.; Anzai, M.; Mori, N.; Kawasaki, H. Controlled aggregation of methylene blue in silica–methylene blue nanocomposite for enhanced $^1O_2$ generation. *Colloids Surf. A Physicochem. Engin. Aspects* **2021**, *617*, 126360. [CrossRef]
39. Toum Terrones, Y.; Torresán, M.F.; Mirenda, M.; Rodríguez, H.B.; Wolosiuk, A. Photoactive Red Fluorescent SiO_2 Nanoparticles Based on Controlled Methylene Blue Aggregation in Reverse Microemulsions. *Langmuir* **2022**, *38*, 6786–6797. [CrossRef]
40. Linger, C.; Lancel, M.; Port, M. Evaluation of relative efficiency of PDT photosensitizers in producing hydroxyl radicals and singlet oxygen in aqueous media using a UV–visible spectroscopy pNDA dosage. *J. Photochem. Photobiol. B* **2023**, *241*, 112664. [CrossRef]
41. Thorning, F.; Henke, P.; Ogilby, P.R. Perturbed and Activated Decay: The Lifetime of Singlet Oxygen in Liquid Organic Solvents. *J. Amer. Chem. Soc.* **2022**, *144*, 10902–10911. [CrossRef] [PubMed]
42. Karimi, S.; Bahri-Laleh, N.; Pareras, G.; Sadjadi, S.; Nekoomanesh-Haghighi, M.; Poater, A. Pd on nitrogen rich polymer–halloysite nanocomposite as an environmentally benign and sustainable catalyst for hydrogenation of polyalfaolefin based lubricants. *J. Ind. Eng. Chem.* **2021**, *97*, 441–451. [CrossRef]
43. Poater, A.; Moradell, S.; Pinilla, E.; Poater, J.; Sola, M.; Martinez, M.A.; Llobet, A. A trinuclear Pt(II) compound with short Pt-Pt-Pt contacts. An analysis of the influence of π-π stacking interactions on the strength and length of the Pt-Pt bond. *Dalton Trans.* **2006**, *9*, 1188–1196. [CrossRef] [PubMed]
44. Frisch, M.J.; Trucks, G.W.; Schlegel, H.B.; Scuseria, G.E.; Robb, M.A.; Cheeseman, J.R.; Scalmani, G.; Barone, V.; Petersson, G.A.; Nakatsuji, H.; et al. *Gaussian 16 Rev. B.01*; Gaussian Inc. Company: Wallingford, CT, USA, 2016.
45. Becke, A.D. Density-functional thermochemistry. III. The role of exact exchange. *J. Chem. Phys.* **1993**, *98*, 5648–5652. [CrossRef]
46. Lee, C.; Yang, W.; Parr, R.G. Development of the Colle-Salvetti correlation-energy formula into a functional of the electron density. *Phys. Rev. B* **1988**, *37*, 785–789. [CrossRef] [PubMed]
47. Stephens, P.J.; Devlin, F.J.; Chabalowski, C.F.; Frisch, M.J. Ab Initio Calculation of Vibrational Absorption and Circular Dichroism Spectra Using Density Functional Force Fields. *J. Phys. Chem.* **1994**, *98*, 11623–11627. [CrossRef]
48. Grimme, S.; Antony, J.; Ehrlich, S.; Krieg, H. A consistent and accurate ab initio parametrization of density functional dispersion correction (DFT-D) for the 94 elements H-Pu. *J. Chem. Phys.* **2010**, *132*, 154104. [CrossRef] [PubMed]
49. Weigend, F.; Ahlrichs, R. Balanced basis sets of split valence, triple zeta valence and quadruple zeta valence quality for H to Rn: Design and assessment of accuracy. *Phys. Chem. Chem. Phys.* **2005**, *7*, 3297–3305. [CrossRef] [PubMed]

50. Weigend, F. Accurate Coulomb-fitting basis sets for H to Rn. *Phys. Chem. Chem. Phys.* **2006**, *8*, 1057–1065. [CrossRef] [PubMed]
51. Marenich, A.V.; Cramer, C.J.; Truhlar, D.G. Universal solvation model based on solute electron density and on a continuum model of the solvent defined by the bulk dielectric constant and atomic surface tensions. *J. Phys. Chem. B* **2009**, *113*, 6378–6396. [CrossRef] [PubMed]

Disclaimer/Publisher's Note: The statements, opinions and data contained in all publications are solely those of the individual author(s) and contributor(s) and not of MDPI and/or the editor(s). MDPI and/or the editor(s) disclaim responsibility for any injury to people or property resulting from any ideas, methods, instructions or products referred to in the content.